Journal of Laser Applications

Enhanced heating by microdroplet lens in nanoparticle electrospray laser deposition

Cite as: J. Laser Appl. **33**, 012012 (2021); https://doi.org/10.2351/7.0000317
Submitted: 30 November 2020 . Accepted: 30 November 2020 . Published Online: 21 December 2020

Tianyi Li, Ranganathan Kumar, and Aravinda Kar

Journal of Laser Applications ARTICLE scitation.org/journal/jla

Enhanced heating by microdroplet lens in nanoparticle electrospray laser deposition

Cite as: J. Laser Appl. 33, 012012 (2021); doi: 10.2351/7.0000317
Submitted: 30 November 2020 · Accepted: 30 November 2020 ·
Published Online: 21 December 2020

Tianyi Li,[1] Ranganathan Kumar,[1] and Aravinda Kar[2]

AFFILIATIONS

[1]Department of Mechanical Engineering, University of Central Florida, Orlando, Florida 32816
[2]CREOL, The College of Optics and Photonics, University of Central Florida, Orlando, Florida 32816

Note: Paper published as part of the special topic on Proceedings of the International Congress of Applications of Lasers & Electro-Optics 2020.

ABSTRACT

In this paper, an additive manufacturing process has been used to deposit nanoparticles on a substrate. In this innovative technique called the nano-electrospray laser deposition process, droplets of various nanosuspensions are dispensed onto a silicon substrate where subwavelength structures and bouncing droplets have been observed. An analytical model is presented for determining the temperature distribution in the substrate by considering the microdroplet as a ball lens. This lens continuously changes the focus of the laser beam as the droplet travels toward the substrate. The laser is either defocused or focused on the substrate forming locally decreased or enhanced heating near the center of the laser beam depending on the distance of the droplet from the substrate. It is found that the enhancement in heating differs for the nanosuspensions since their optical properties are different. The subwavelength structures determined from the post-pulse temperature qualitatively match with the experimental results. The steady end-period temperature is also compared with the experimentally observed temperature for bouncing droplets and the temperatures are in good agreement.

Key words: pulsed laser deposition, laser-microdroplet interaction, microdroplet lens, Bessel beam heating, temperate modeling, analytical solution, electrospray, optical absorption

I. INTRODUCTION

Nano-Electrospray Laser Deposition (NELD) is a newly developed additive manufacturing method, which uses nanoparticle suspension, to print nanopatterns or micropatterns on substrates in nanophotonic or optoelectronic devices.[1] The nanoparticles have better mechanical, electrical, and optical properties as well as lower melting temperature compared to their bulk material counterpart.[2] In NELD, an aqueous suspension of nanoparticles, e.g., silver nanoparticle suspension, is used as a precursor to produce microdroplets by an electrospray method. The suspension is fed to a positively charged capillary tube using a syringe pump, and the microdroplets are extracted from the tip of the tube using a negatively charged electrode. The droplets pass through a hollow parabolic mirror and enter into a hollow conical laser beam to eventually interact with a Bessel laser beam at the apex of the cone where the laser evaporates the liquid and sinters the nanoparticles on the substrate.[3–5] The laser–droplet interaction occurs in mid-air as well as on the substrate, creating subwavelength structures on the substrate.[6]

The microdroplets respond to laser heating differently depending on the laser power. Research on such droplet heating on hot surfaces has gained some attention recently.[7–11] The bouncing of droplets from Si substrates under high laser power is also observed experimentally, which is similar to the droplet rebounding from a hot surface, known as the Leidenfrost effect.[12,13] Shirota *et al.* experimentally studied the effect of an isothermal surface temperature on the time and length scales of the Leidenfrost boiling of droplets.[14] Villegas *et al.* numerically simulated the droplet impingement on a hot surface for Weber numbers ranging from 7 to 45 at temperatures well above the Leidenfrost point.[15] It is commonly accepted that the dynamics of a droplet impinging on a hot surface depends predominantly on the temperature of the surface.[16–19]

The substrate surface temperature during laser heating is, therefore, a significant variable for understanding different phenomena

that may arise when the droplets impinge on the substrate. Yilbas and Shuja compared the temperature distributions due to short-pulse laser heating by considering three models: the Fourier heating, two equations for electron and lattice heating, and kinetic theory models[20] and inferred that the Fourier model is not applicable for laser pulses shorter than 0.1 ns. Yilbas and Pakdemirli also presented a closed-form solution for the temperature distribution due to pulsed laser heating by solving the hyperbolic heat conduction equation using a perturbation method.[21,22] Nath *et al.*[23] considered a one-dimensional model for the temperature profiles during heating and cooling cycles, resulting from laser pulse on–off times, and analyzed the effects of various processing parameters, such as the laser power, beam diameter, scan speed, pulse duration, pulse repetition rate, and duty cycle, on laser surface hardening. Chen *et al.*[24] and Taylor *et al.*[25] developed the two-dimensional and three-dimensional analytical solutions for pulsed laser heating of aluminum and silicon substrates, respectively. A generalized analytical solution was developed by Lam for electron and lattice temperature profiles in a metallic film exposed to ultrashort laser pulses using the superposition of temperature and the Fourier transform method in conjunction with the solution structure theorems.[26] In the application of laser manufacturing, Rahaman *et al.*[27] solved the Fourier heat conduction equation analytically using an integral transform technique for the temperature distribution in polypropylene due to femtosecond laser heating, and they demonstrated that their model predictions agree well with the experimental results.

An analytical two-dimensional, transient heat conduction model is developed in the present paper, to predict the temperature distribution in the substrate due to the Bessel laser heating during the NELD process. A pulsed Nd:YAG laser of 1064 nm wavelength is illuminated on a silicon substrate through microdroplets of different nanoparticle suspension as the droplets fall down onto the substrate. The microdroplet serving as a ball lens focuses the laser beam on the silicon substrate, and therefore the laser irradiance distribution on the substrate surface continuously changes as the distance between the droplet and the substrate decreases. Consequently, enhanced heating can occur at the center of the laser beam, resulting in subwavelength structures on the substrate. The predictions of the analytical solution are verified using the experimental results on different droplets impinging on a silicon substrate.

II. METHODOLOGY

The analytical solution for the model of this study is presented in this section. Shown in Fig. 1 is the schematic of the model and the axisymmetric cylindrical coordinate (r', z') system used to describe the laser propagation as well as the axisymmetric cylindrical coordinate (r, z) system used to calculate the temperature distribution in Si substrates. With the nanoparticle suspension droplet falling down, the pulsed Nd:YAG laser is refocused by the droplet and the laser irradiance on the substrate changes continuously. The radius and speed of each droplet are set as $\rho_0^* = 50\,\mu$m and $v = 2$ m/s, respectively, since these data correspond to the experimental results[5] that are used in this study for model verification. The substrate is a thin Si wafer of radius $r_0 = 25$ mm and thickness $L = 0.4$ mm in the r and z directions, respectively. The absorbed laser energy is assumed to be converted to heat instantaneously.

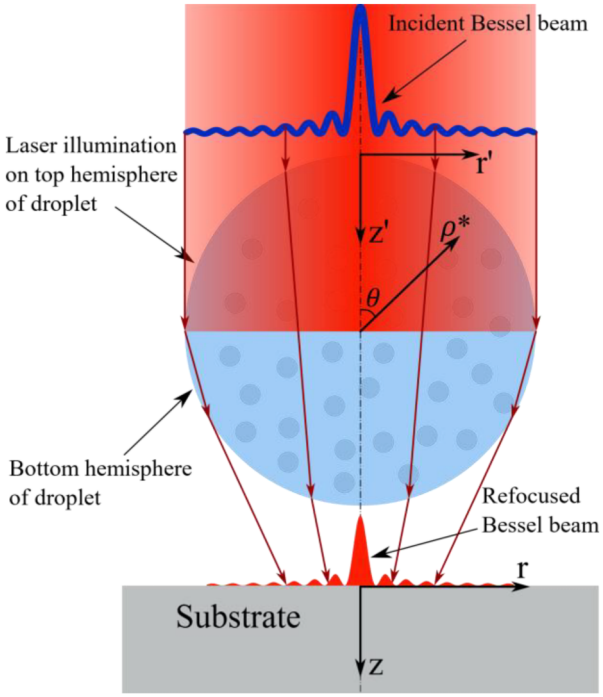

FIG. 1. Schematic of a laser passing through a droplet and heating a substrate in a cylindrical coordinate system. Center of the laser is aligned with the center of the droplet and center of the Si substrate at $r = 0$. The laser is distributed in ther' direction and propagating in the z' direction. The droplet is described by spherical coordinates with radial distance ρ^* and polar angle θ.

A. Bessel beam propagation in microdroplet lens

The zeroth order Bessel function of the first kind, J_0, represents a nondiffracting beam[28] whose intensity distribution remains the same in every plane perpendicular to the direction of the propagation, z' axis (Fig. 1). This ideal beam is, however, difficult to achieve in practice due to the diffraction effect of a finite aperture. Indebetouw[29] showed that approximately nondiffracting beam can be synthesized using an axicon lens. The intensity distribution of these nonideal or real beams varies along the z' axis.[30] This variation is considered very small in this study since the diameter of each droplet is $\sim 100\,\mu$m and the laser–droplet interaction occurs over a very small distance of $\sim 500\,\mu$m above the substrate surface and, therefore, only the radial component of the intensity distribution is used in the following analysis. Under this assumption, the irradiance distribution of a pulsed Bessel beam incident on the top surface of the droplet can be written as

$$I_{\text{orig}}(r', t) = I_0 J_0^2(k_{r'} r') \phi(t), \tag{1}$$

where r' is the radial distance from the center of the beam and t is the time variable for the temporal shape of the laser pulse. $k_{r'}$ is the radial wave vector given by $k_{r'} = \sqrt{(2\pi/\lambda)^2 - k_{z'}^2}$, where $k_{z'}$ is the wave vector in the laser beam propagation direction z' (Fig. 1) and λ is the

laser wavelength which is 1064 nm in this study. For $0 < k_{r'} \le 2\pi/\lambda$, the laser is a nondiffracting beam in which the envelope of the maxima in the intensity distribution (Fig. 1) decreases radially and this variation of the envelope is inversely proportional to $k_{r'}r'$. The effective diameter of the beam is determined by $k_{r'}$ and the central high intensity spot reduces to its minimum possible diameter 0.77λ when $k_{r'} = 2\pi/\lambda$. $k_{r'}$ is taken as $2\pi/\lambda$ in this study. $\phi(t)$ is the temporal distribution of the irradiance due to the laser pulse:

$$\phi(t) = \begin{cases} \dfrac{t-(n_p-1)t_p}{0.5t_{on}}, & (n_p-1)t_p \le t \le (n_p-1)t_p + 0.5t_{on}, \\ \dfrac{t_{on}+(n_p-1)t_p-t}{0.5t_{on}}, & (n_p-1)t_p + 0.5t_{on} < t \le (n_p-1)t_p + t_{on}, \\ 0, & (n_p-1)t_p + t_{on} < t < n_p t_p, \end{cases} \tag{2}$$

where $n_p = 1, 2, 3, \ldots$ are the total number of pulses irradiating the substrate after passing through the droplet and t_{on} and t_p are the laser pulse on-time and laser period, respectively. t_p is the sum of the pulse on and off times. Schematic of $\phi(t)$ is shown in Fig. 2.

I_0 is the peak intensity of the Bessel laser beam incident on the top surface of the droplet and it can be calculated from the laser power P as

$$I_0 = \frac{2P}{p_{rf} t_{on} \pi R_l^2 [J_0^2(k_{r'}R_l) + J_0^2(k_{r'}R_l)]}, \tag{3}$$

where the laser pulse repetition frequency $p_{rf} = 30$ kHz and the radius of the incident beam $R_l = 150\ \mu$m, which correspond to the data used in the Nano-Electrospray Laser Deposition experiment.[5]

The laser refraction due to the droplet is shown in Fig. 3. When the distance between the droplet and the substrate surface, $H(t)$, is larger than the diameter of the droplet, the laser intensity distribution refracted by the droplet can be calculated by using the following equations. The incidence angle for laser ray at $w_{in} = \rho_0^* \sin\theta_1$ is θ_1. The reflected angle can be written as $\theta_2 = \arcsin(\sin\theta_1/n)$. The corresponding laser ray location beneath the droplet at H can be written as

$$w(t) = \frac{[((R_0 \sin\theta_1)/(\sin(2\theta_1 - 2\theta_2))) - H(t)]\sin(2\theta_2 - \theta_1)}{((\sin\theta_1)/(\sin(2\theta_1 - 2\theta_2))) - \cos(2\theta_2 - \theta_1)}. \tag{4}$$

And, the laser intensity at this point can be expressed as

$$I(r = w, t) = \frac{w_{in}^2}{w(t)^2}(1 - R_d) I_{orig}(w_{in}, t) e^{-\eta d(\theta_2)}, \tag{5}$$

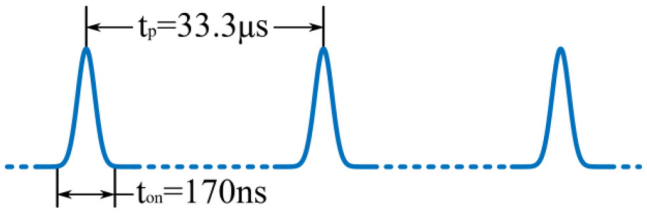

FIG. 2. Schematic of the pulsed laser pattern. The period of the laser is $t_p = 33.3\ \mu$s, corresponding to 30 kHz repetition frequency and the pulse on-time is $t_{on} = 170$ ns.

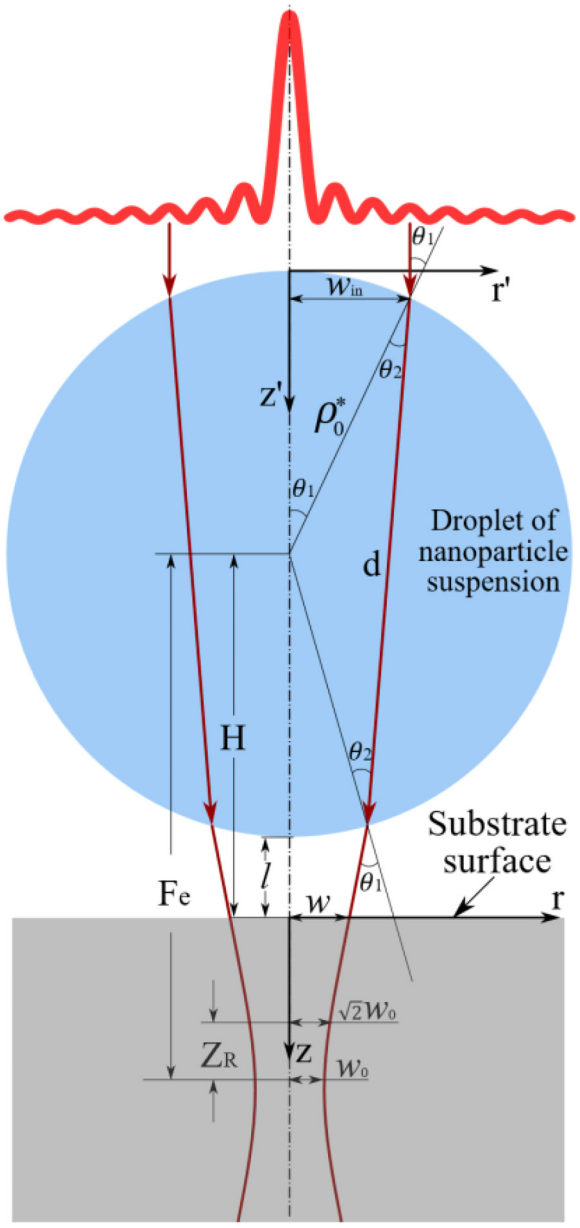

FIG. 3. Schematic of laser refraction by a droplet.

where

$$d(\theta_2) = 2\rho_0^* \cos\theta_2. \tag{6}$$

When the distance between the droplet and the substrate surface, $H(t)$, is less than the diameter of the droplet, the laser intensity on the Si substrate after passing droplet can be

TABLE I. Fluid and optical properties of nanoparticle suspensions at laser wavelength λ = 1064 nm.

Sample ID	Density ρ (g/ml)	Viscosity μ (cP)	Surface tension σ (mN/m)	Reflectance R_d (%)	Absorption coefficient η (cm^{-1})	Refractive index n
Ag20	1.153	1.71	47.2	6	100	1.377
SDS	1.000	1.10	49.8	48	0.2	1.330
Ge5	1.064	1.56	47.5	42	4.17	1.340
Ge10	1.130	1.95	47.6	35	7.7	1.358
Si5	1.033	1.82	48.2	28	6.25	1.348

estimated as[31]

$$I(r,t)=\frac{w_{inc}^2}{w_c(t)^2}(1-R_d)e^{-2\eta\rho_0^*}I_0 J_0^2\left(k_{r^*}\frac{w_{inc}}{w_c(t)}\,r\right)\phi(t), \tag{7}$$

where R_d and η are the reflectance and absorption coefficients listed in Table I. ρ_0^* represents the radius of the droplet, and w_{inc} is the laser incidence radius assumed to be 150 μm. w_c is the focused laser spot radius on the Si substrate, which can be expressed as

$$w_c(t)=w_0\sqrt{1+\left(\frac{F_e-H(t)}{z_R}\right)^2}, \tag{8}$$

where w_0 is the spot radius at the focal point, which is given by

$$w_0=\frac{n\cdot\rho_0^*\cdot\lambda}{8(n-1)w_{in}}, \tag{9}$$

with n representing the refractive index of the microdroplets. z_R is the Rayleigh range,

$$z_R=\frac{\pi w_0^2}{\lambda}. \tag{10}$$

F_e is the distance between the focal point and the droplet center for laser passing the droplet axis,

$$F_e=\frac{nR_0}{2(n-1)}. \tag{11}$$

B. Effect of microdroplet lens on the substrate temperature

The modified irradiance distribution caused by the microdroplet lens is used to determine the temperature in a substrate, which is assumed to be initially in the ambient temperature, $T_{amb}=25\,^{\circ}$C. The laser irradiance on the substrate is assumed to be a direct heat flux into the substrate. The substrate is considered to be sufficiently large in the radial direction so that the temperature at the edge of the substrate can be approximated to be T_{amb} which is in good agreement with a convective boundary condition.[27] The governing equation, boundary conditions, and initial condition for the temperature, $T(r,z,t)$, in the substrate can be written as follows in terms of the excess temperature $T^*(r,z,t)=T(r,z,t)-T_{amb}$:

$$\frac{\partial^2 T^*}{\partial r^2}+\frac{1}{r}\frac{\partial T^*}{\partial r}+\frac{\partial^2 T^*}{\partial z^2}=\frac{1}{\alpha}\frac{\partial T}{\partial t}, \tag{12}$$

$$BC1:\ \frac{\partial T^*}{\partial r}\Big|_{r=0}=0, \tag{13}$$

$$BC2:T^*(r=r_0)=0, \tag{14}$$

$$BC3:hT^*(z=L)+k\frac{\partial T^*}{\partial z}\Big|_{z=L}=0, \tag{15}$$

$$BC4:\ hT^*(z=0)-k\frac{\partial T^*}{\partial z}\Big|_{z=0}=(1-R_s)I(r,t), \tag{16}$$

$$IC:\ T^*(t=0)=0. \tag{17}$$

Here, the thermal diffusivity $\alpha=0.8\ cm^2/s$, the thermal conductivity $k=119$ W/mK, and the reflectivity $R_S=0.3$ for Si.[32] The overall heat convection coefficient is taken to be $h=100$ W/mK within the natural convection coefficient range of $10-1000$ W/mK.

Equation (12) is solved using the following finite medium Hankel transform[33] pairs in the radial direction:

$$\begin{cases}\overline{T^*}(\eta_i,z,t)=\int_{r''=0}^{r_0} r''J_0(\eta_i r'')T^*(r'',z,t)\,dr'',\\ T^*(r,z,t)=\sum_{i=1}^{\infty}\frac{J_0(\eta_i r)}{N(\eta_i)}\overline{T^*}(\eta_i,z,t),\end{cases} \tag{18}$$

where η_i is the ith eigenvalue, which is determined by Eq. (10) as $J_0(\eta_i r_0)=0$, and $N(\eta_i)$ is the norm of the eigenfunction $J_0(\eta_i r)$ with the weighting function r, which is given by

$$N(\eta_i)=\int_{r''=0}^{r_0} r''J_0^2(\eta_i r'')\,dr'=\frac{1}{2}r_0^2J_1^2(\eta_i r_0). \tag{19}$$

The governing equation (12), boundary conditions (15) and (16), and initial condition (17) can be expressed as follows in terms of the Hankel transform temperature $\overline{T^*}(\eta_i,z,t)$:

$$-\eta_i^2\overline{T^*}+\frac{\partial^2\overline{T^*}}{\partial z^2}=\frac{1}{\alpha}\frac{\partial\overline{T^*}}{\partial t}, \tag{20}$$

$$h\overline{T^*} + k\frac{\partial \overline{T^*}}{\partial z}|_{z=L} = 0, \tag{21}$$

$$h\overline{T^*} - k\frac{\partial \overline{T^*}}{\partial z}|_{z=0} = \bar{I}(\eta_i,\ t), \tag{22}$$

$$\overline{T^*}(t=0) = 0, \tag{23}$$

where

$$\bar{I}(\eta_i,\ t) = \int_{r''=0}^{r_0} r'' J_0(\eta_i r'') I(r'',\ t)\, dt. \tag{24}$$

Equation (24) is solved using the following finite medium Fourier transform[33] pairs in the z-direction:

$$\begin{cases} \widetilde{T^*}(\eta_i,\ \beta_j,\ t) = \int_{Z'=0}^{L} Z_j(z'')\overline{T^*}(\eta_i,\ z'',\ t)\, dz'', \\ \overline{T^*}(\eta_i,\ z,\ t) = \sum_{j=1}^{\infty} \frac{Z_j(z)}{N(\beta_j)} \widetilde{T^*}(\eta_i,\ \beta_j,\ t), \end{cases} \tag{25}$$

where $Z_j(z)$ is the eigenfunction,

$$Z_j(z) = \beta_j \cos\beta_j z + \frac{h}{k}\sin\beta_j z, \tag{26}$$

with the eigenvalue β_j given by

$$\tan\beta_j L = \frac{2h\beta_j}{k\beta_j^2 - (h^2/k)}, \tag{27}$$

and $\tilde{N}(\beta_j)$ is the norm of the eigenfunction $Z_j(z)$,

$$\tilde{N}(\beta_j) = \frac{1}{2}\left(\beta_j^2 + \frac{h^2}{k^2}\right)L + \frac{h}{k}. \tag{28}$$

Equation (20) and initial condition (23) can be expressed as follows in terms of the Hankel–Fourier transform temperature $\widetilde{T^*}(\eta_i,\ \beta_j,\ t)$:

$$-(\eta_i^2 + \beta_j^2)\widetilde{T^*} + \beta_j \frac{\bar{I}(\eta_i, t)}{k} = \frac{1}{\alpha}\frac{\partial \widetilde{T^*}}{\partial t}, \tag{29}$$

$$\widetilde{T^*}(\eta_i, \beta_j, t=0) = 0. \tag{30}$$

The solution of Eq. (29) under initial condition (30) is given by

$$\widetilde{T^*} = \frac{\alpha}{k}\int_{\tau=0}^{t} \beta_j \bar{I}(\eta_i,\ \tau) e^{-\alpha(\eta_i^2+\beta_j^2)(t-\tau)}\, d\tau. \tag{31}$$

The inverse Fourier transforms is applied to Eq. (31) to obtain $\overline{T^*}(\eta_i,\ z,\ t)$ and then the inverse Hankel transform is applied to $\overline{T^*}(\eta_i,\ z,\ t)$ to determine T^*,

$$T^*(r, z, t) = \frac{\alpha}{k}\sum_{i=1}^{\infty}\frac{J_0(\eta_i r)}{N(\eta_i)}\sum_{j=1}^{\infty}\frac{Z_j(z)}{N(\beta_j)}\widetilde{T^*}(\eta_i, \beta_j, t). \tag{32}$$

The actual temperature distribution in the substrate is obtained using the relation $T = T^* + T_{amb}$, which is used to analyze the effect of the microdroplet lens on laser heating of the substrate.

III. RESULTS AND DISCUSSION

The perturbed irradiance distributions of the laser on the Si substrate are shown in Fig. 4 at different times, i.e., for different heights of the droplets from the substrate. The laser is defocused on the substrate when the droplets just enter the diffraction-free region around the apex of the laser cone at $t = 0$. The peak intensity, I_0, on the substrate decreases compared to the peak intensity of the laser beam incident on the top surface of the droplet. This perturbation in the intensity is due to the absorption and refocusing by the droplets. In addition, the height of the droplet bottom from the substrate surface, $H(t)$ decreases as the droplets drop at the speed of 2 m/s, and consequently, the focal spot size on the substrate gradually decreases to yield a maximum I_0 when the droplet bottom is $41.5 - 51\ \mu$m above the substrate. This height depends on the optical properties of the nanoparticle suspension droplets, such as the refractive index and absorption coefficient as listed in Table I.

In addition to altering the peak intensity, the droplet lens modifies the spatial profile of the laser irradiance distribution. Shown in Fig. 5 are the laser profiles on the substrate at different times for Ag20 droplets. When $t < 180\ \mu$s, the laser profile is stretched due to defocusing by the Ag20 droplet. When $t > 203\ \mu$s, the peak intensity obtained on the substrate with the droplet is larger than the peak intensity without any droplet. This result indicates that enhanced heating can occur around the center ($r = 0$) of the laser spot.

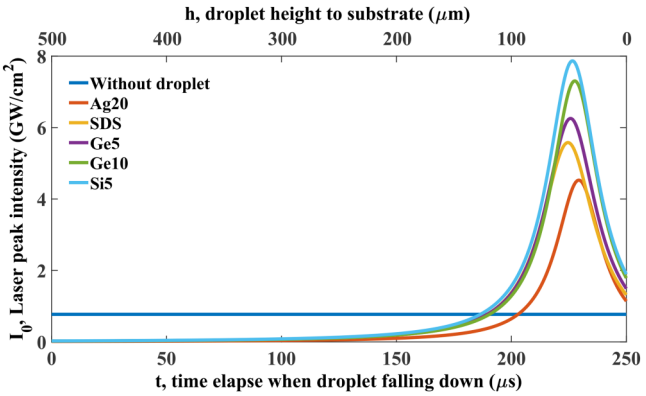

FIG. 4. Laser peak intensity on the Si substrate for different nanoparticle suspension droplets during transit from the diffraction-free zone to the substrate.

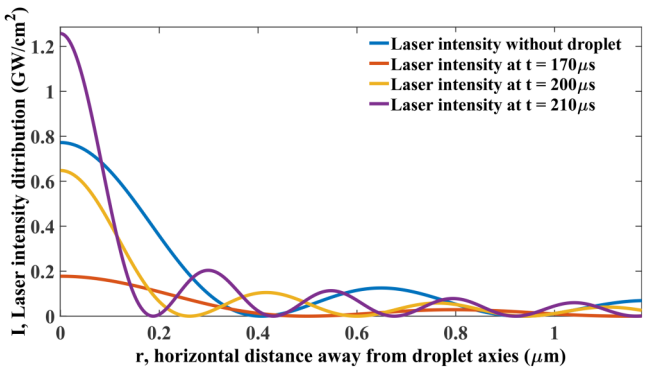

FIG. 5. Laser intensity profile on the Si substrate for Ag20 droplets at different transit times.

The temperature at the laser spot center is calculated for the laser power, $P = 9\ W$, to determine the enhancement in heating due to different suspension droplets. The convection coefficient h and the reflectance of substrate R_s are set to be 10^5 W/mK and 0.6, respectively, to introduce the decrease in laser heating of the Si substrate due to the liquid in droplets on the Si surface. Figure 6 compares the temperature at $r = 0$ as a function of time when the droplet is absent or present in the path of the laser beam. A steep increase and decrease in temperature can be observed for all cases during each period of the pulse. The temperature rises rapidly due to the rapid heating during the laser pulse-on time. $t_{on} = 170$ ns. During the pulse-off time, the heat diffuses rapidly in the Si substrate and also the substrate is cooled by convection cooling which decreases the surface temperature rapidly.

For direct heating of the substrate without any droplet, however, the peak temperature remains the same for all pulses

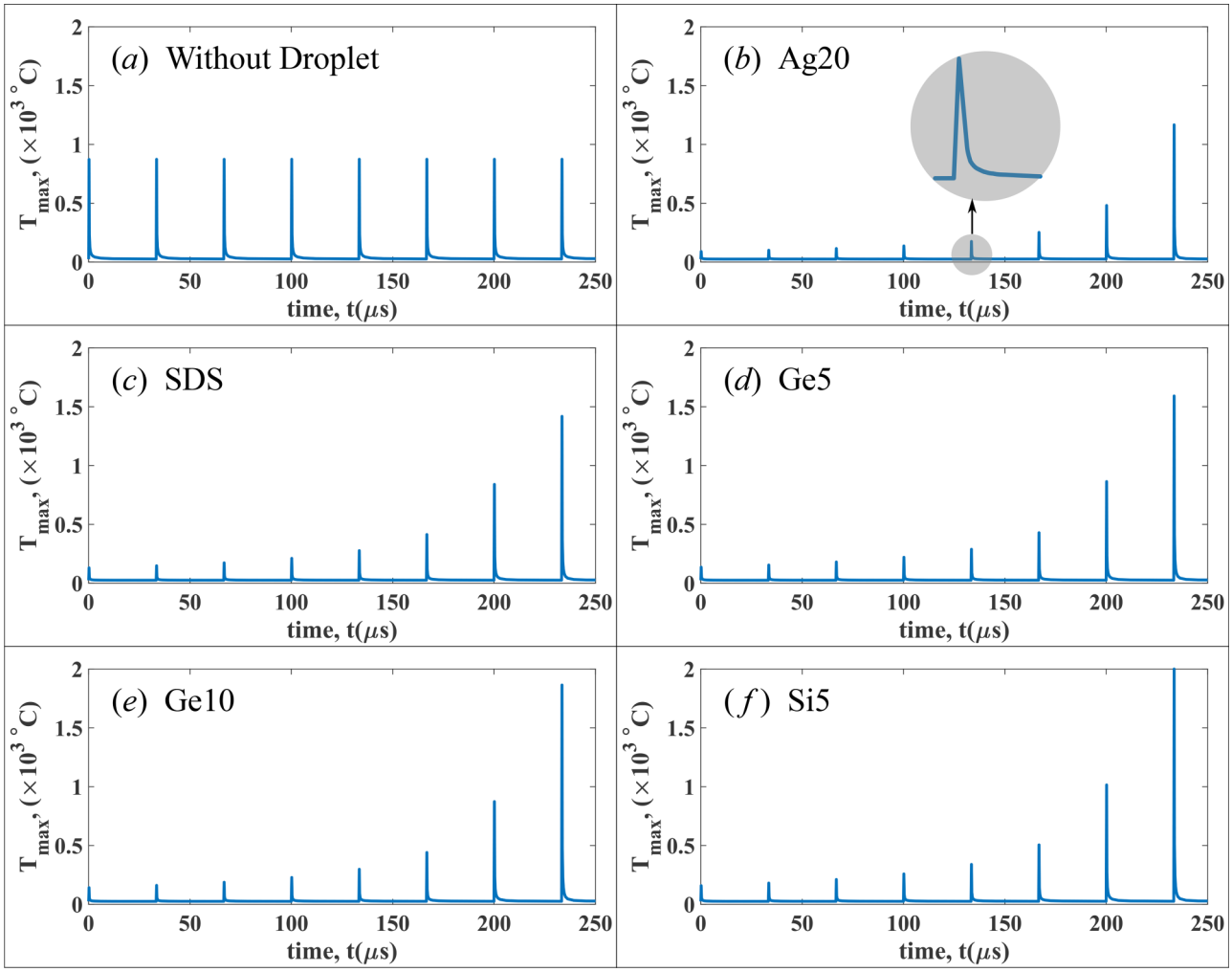

FIG. 6. Laser induced maximum temperature on Si substrates vs time with and without nanoparticle suspension droplets for $P = 9$ W, $h = 10^5$ W/mK, and $R_s = 0.6$.

[Fig. 6(a)]. For transit time $t \leq 180\ \mu s$, i.e., when the droplet is more than 140 μm above the substrate, the laser beam is defocused and consequently the substrate temperature is lower than the direct heating case [Fig. 6(a)] for all cases. For transit time $t \geq 203\ \mu s$, i.e., when the droplet is less than 100 μm above the substrate, the laser beam is refocused and consequently the substrate temperature is higher than the direct heating case [Fig. 6(a)] for all cases. This defocusing and refocusing effects cause the reduction and enhancement in the laser intensity as shown in Fig. 4. Also, the above transit time limits exhibit an interval of 23 μs because the droplets of different optical properties refocus the laser beam at different times (Fig. 4).

Eduardo *et al.*[5] created subwavelength holes of average sizes 100, 500, and 800 nm on Si substrates using SDS, Ge5, and Ge10 droplets, respectively, a laser power of 9 W on each droplet. The temperature distributions are plotted in Fig. 7 for these three and Ag20 droplets at transit time $t = 233.5\ \mu s$, which is just after the seventh pulse and before the droplet impingement on the substrate. Ag20, Ge10, Ge5, and SDS droplets have absorption coefficients in the descending order as listed in Table I, and all of these droplets focus the laser to enhance heating as illustrated in Fig. 6. Due to their different absorption coefficients, the local enhancement in laser heating varies. Ag20 droplets absorb more laser energy due to their higher absorption coefficient than the other three types of droplets. Less laser energy, therefore, exits the Ag20 droplets, resulting in lower temperatures of the substrate than the other three cases as shown by the color temperature maps in Fig. 7. Figures 7(b)–7(d) show the Si melting temperature isotherm 1414 °C above which the material is considered to vaporize in this study to form a hole in the substrate. The Ag20 sample in Fig. 7(a), on the other hand, does not exhibit the isotherm 1414 °C, indicating no hole formation in this sample. This prediction is in agreement with the experimental observation[34] of no holes in the Si substrate for the case of Ag20 droplets.

For the other samples in Fig. 7, the isotherm 1414 °C is deeper for the Ge10 sample and progressively becomes shallower for Ge5 and SDS samples. The hole sizes in this figure are 60, 1500, and 2500 nm for SDS, Ge5, and Ge10, respectively, while the corresponding experimental data[5] are 100, 500, and 800 nm. The theoretical and experimental hole sizes are comparable for the SDS sample, but the sizes differ significantly for the other two samples. This discrepancy may be due to the same liquid convection coefficient, 10^5 W/mK, used for these cases. The liquid convection coefficient of 10^5 W/mK may be applicable to the SDS droplets. However, Ge5 and Ge10 droplets contain 5 and 10 wt. % germanium nanoparticles, respectively, and the thermal conductivity of these nanoparticles is expected to increase the overall liquid convection coefficient higher than 10^5 W/mK. The usage of 10^5 W/mK, therefore, underestimates the convection heat loss and overestimates the laser heating of the substrate, resulting in a deeper melting isotherm and larger hole size.

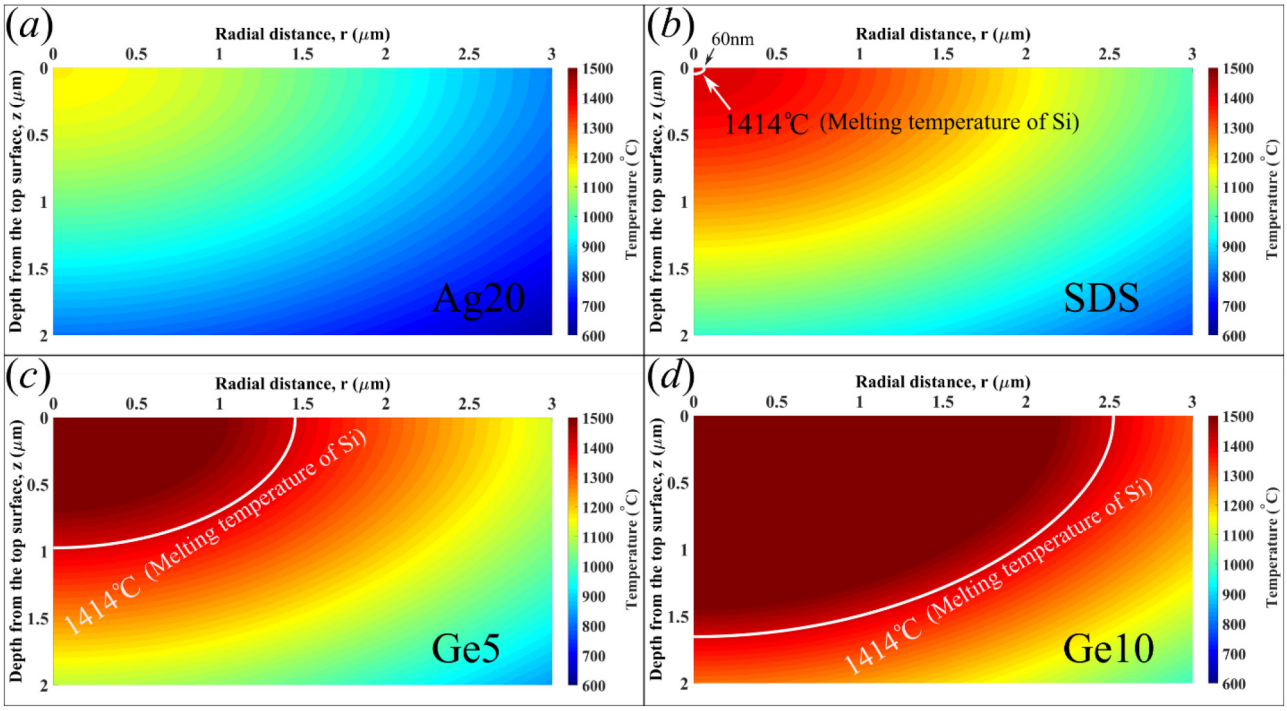

FIG. 7. Temperature profiles in an Si substrate induced by laser through nanoparticle suspension droplets at transit time $t = 233.5\ \mu s$ for $P = 9$ W, $h = 10^5$ W/mK, and $R_s = 0.6$. (a) Ag20, (b) SDS, (c) Ge5, and (d) Ge10.

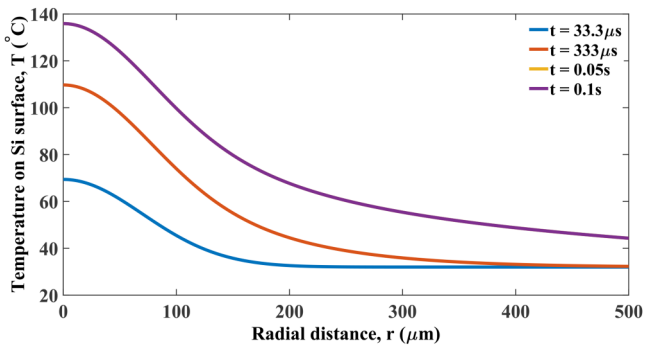

FIG. 8. Temperature profile on the Si substrate surface at different times with laser power $P = 22$ W. The time is picked at the end of the pulse period.

When the laser power is increased from 9 to 22 W, the droplets are observed to bounce back to air from the substrate, known as the Leidenfrost effect, where the surface temperature plays an important role. Compared to the laser pulse repetition frequency, $p_{rf} = 30$ kHz, the droplet frequency, i.e., the number of droplets delivered to the substrate per unit time, is much less ($f_{\text{drop}} = 420$ Hz), which indicates that the laser illuminates the substrate most of the time without passing through any droplet. The temperature profiles on the substrate surface are plotted in Fig. 8 at different times. Each profile is calculated at the end of one period (pulse-on time + pulse-off time) of the pulse train to allow the maximum relaxation time for the thermal energy to diffuse in the substrate. This procedure yields the minimum temperature profile, called the end-period temperature, which increases with time when more and more pulses illuminate the substrate. Eventually, the temperature reaches a steady state when the input laser energy is equal to the diffusion loss of thermal energy, which is found to occur at $t \geq 0.05$ s in this study.

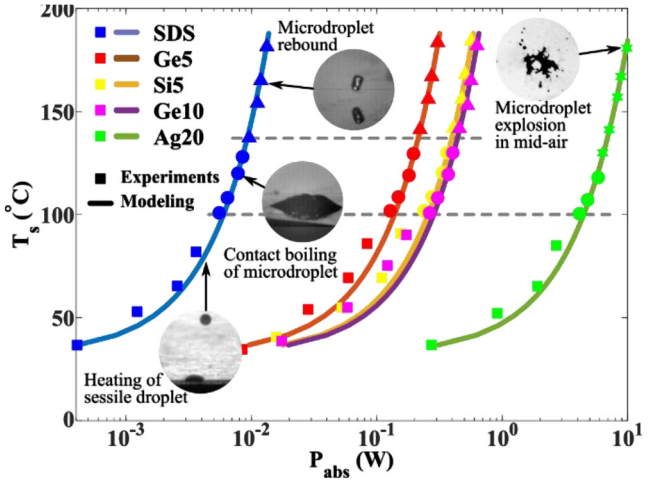

FIG. 9. Comparison between analytical solution and experiments for substrate surface temperature vs absorbed power.

The end-period temperatures at the laser spot center are calculated at $t = 0.1$ s and plotted in Fig. 9 as a function of absorbed laser power. The experimental data in this figure show that the droplet bouncing regime (Leidenfrost condition) occurs above the temperature T = 137 °C. The temperatures predicted by the model in this regime match with the experimental data[34] very well since the droplets do not form sessile drops on the substrate surface in this regime, and the analytical model is also based on droplets that do not break into sessile drops. However, Fig. 9 shows that the temperatures predicted by the model are less than the experimental temperatures in the laser heating and boiling regimes. This discrepancy may be ascribed to the existence of sessile drop on the surface in these two regimes, whereas the model considers only spherical droplets. In addition, the convection heat transfer coefficient (h) in the model may be slightly higher than that of the sessile drop in the experiment.

IV. CONCLUSION

An analytical model is developed to analyze the effect of microdroplet ball lens on laser heating of a substrate when the droplets carry nanoparticles for potential deposition of thin films on the substrate. The model can be applied to calculate two-dimensional, transient temperature distributions in the substrate. The nanoparticle suspension droplets can either decrease or increase the temperature around the center of the laser spot on the substrate by defocusing or focusing the laser, respectively. This lens effect of the droplets depends on the reflectance, absorption coefficients, and refractive index of the nanosuspension, and the resulting variation in the laser irradiance distribution on the substrate surface depends on the height of the droplets above the substrate. Droplets with lower reflectance or absorption coefficient and higher refractive index enhance laser heating of the substrate. The post-pulse temperature distribution due to laser heating enhancement has been evaluated for different types of nanoparticle suspension droplets, and the diameter of the high temperature region is found to qualitatively match with the size of subwavelength structures induced by the laser on Si substrates. The effect of illuminating the Si substrate for a long time is also modeled as the steady end-period temperature to determine the conditions for droplets to bounce off the substrate, and this end-period temperature matches with the droplet–substrate interaction regime map including the microdroplet bouncing regime for different laser powers.

This analytical model can be used to predict the formation of subwavelength structures on a substrate due to enhanced laser heating or the bouncing of droplets from the substrate due to high surface temperature. These predictions are useful for depositing nanoparticles using nanoparticle suspension droplets.

ACKNOWLEDGMENT

The experimental data are provided by Eduardo Castillo at ESPOL.

REFERENCES

[1]E. Castillo-Orozco, R. Kumar, and A. Kar, "Laser electrospray printing of nanoparticles on flexible and rigid substrates," J. Laser Appl. **31**, 022015 (2019).
[2]P. Buffat and J. Borel, "Size effect on the melting temperature of gold particles," Phys. Rev. A **13**, 2287–2298 (1976).
[3]E. Castillo-Orozco, A. Kar, and R. Kumar, "Electrospray mode transition of microdroplets with semiconductor nanoparticle suspension," Sci. Rep. **7**, 1–10 (2017).
[4]E. Castillo-Orozco, A. Kar, and R. Kumar, "Non-dimensional groups for electrospray modes of highly conductive and viscous nanoparticle suspensions," Sci. Rep. **10**, 1–10 (2020).
[5]E. Castillo-Orozco, R. Kumar, and A. Kar, Proc. SPIE **10667**, 106670M.
[6]E. Castillo-Orozco, R. Kumar, and A. Kar, "Laser-induced subwavelength structures by microdroplet superlens," Opt. Express **27**, 8130–8142 (2019).
[7]P. Eshuis, K. van der Weele, D. van der Meer, and D. Lohse, "Granular leidenfrost effect: Experiment and theory of floating particle clusters," Phys. Rev. Lett. **95**(25), 258001 (2005).
[8]I. V. Roisman, J. Breitenbach, and C. Tropea, "Thermal atomisation of a liquid drop after impact onto a hot substrate," J. Fluid Mech. **842**, 87–101 (2018).
[9]J. Breitenbach, I. Roisman, and C. Tropea, "Drop collision with a hot, dry solid substrate: Heat transfer during nucleate boiling," Phys. Rev. Fluids **2**, 074301 (2017).
[10]G. Liang, X. Mu, Y. Guo, S. Shen, S. Quan, and J. Zhang, "Contact vaporization of an impacting drop on heated surfaces," Exp. Therm. Fluid Sci. **74**, 73–80 (2016).
[11]J. Breitenbach, I. Roisman, and C. Tropea, "Heat transfer in the film boiling regime: Single drop impact and spray cooling," Int. J. Heat Mass Transfer **110**, 34–42 (2017).
[12]B. S. Gottfried, C. J. Lee, and K. J. Bell, "The Leidenfrost phenomenon: Film boiling of liquid droplets on a flat plate," Int. J. Heat Mass Transfer **9**, 1167–1188 (1966).
[13]G. Castanet, T. Liénart, and F. Lemoine, "Dynamics and temperature of droplets impacting onto a heated wall," Int. J. Heat Mass Transfer **52**, 670–679 (2009).
[14]M. Shirota, M. Limbeek, C. Sun, A. Prosperetti, and D. Lohse, "Dynamic Leidenfrost effect: Relevant time and length scales," Phys. Rev. Lett. **116**, 064501 (2016).
[15]L. Villegas, S. Tanguy, G. Castanet, O. Caballina, and F. Lemoine, "Direct numerical simulation of the impact of a droplet onto a hot surface above the Leidenfrost temperature," Int. J. Heat Mass Transfer **104**, 1090–1109 (2017).
[16]T. Mao, D. Kuhn, and H. Tran, "Spread and rebound of liquid droplets upon impact on flat surfaces," AIChE J. **43**, 2169–2179 (1997).
[17]A. Karl and A. Frohn, "Experimental investigation of interaction processes between droplets and hot walls," Phys. Fluids **12**, 785–796 (2000).
[18]H. Fujimoto, O. Yosuke, O. Tomohiro, and T. Hirohiko, "Hydrodynamics and boiling phenomena of water droplets impinging on hot solid," Int. J. Multiph. Flow **36**, 620–642 (2010).
[19]T. Tran, H. Staat, A. Prosperetti, C. Sun, and D. Lohse, "Drop impact on superheated surfaces," Phys. Rev. Lett. **108**, 036101 (2012).
[20]B. S. Yilbas and S. Z. Shuja, "Laser short-pulse heating of surfaces," J. Phys. D Appl. Phys. **32**, 1947–1954 (1999).
[21]B. S. Yilbas and M. Pakdemirli, "Analytical solution for temperature field in electron and lattice sub-systems during heating of solid film," Physica B **382**, 213–219 (2006).
[22]B. S. Yilbas, A. Y. Al-Dweik, and S. Bin Mansour, "Analytical solution of hyperbolic heat conduction equation in relation to laser short-pulse heating," Physica B **406**, 1550–1555 (2011).
[23]A. K. Nath, A. Gupta, and F. Benny, "Theoretical and experimental study on laser surface hardening by repetitive laser pulses," Surf. Coat. Technol. **206**, 2602–2615 (2012).
[24]G. Chen, Y. Wang, J. Zhang, and J. Bi, "An analytical solution for two-dimensional modeling of repetitive long pulse laser heating material," Int. J. Heat Mass Transfer **104**, 503–509 (2017).
[25]L. L. Taylor, R. E. Scott, and J. Qiao, "Integrating two-temperature and classical heat accumulation models to predict femtosecond laser processing of silicon," Opt. Mater. Express **8**, 648–658 (2018).
[26]T. T. Lam, "A generalized heat conduction solution for ultrafast laser heating in metallic films," Int. J. Heat Mass Transfer **73**, 330–339 (2014).
[27]A. Rahaman, A. Kar, and X. Yu, "Thermal effects of ultrafast laser interaction with polypropylene," Opt. Express **27**, 5764–5783 (2019).
[28]J. Durnin, "Exact solutions for nondiffracting beams. I. The scalar theory," J. Opt. Soc. Am. A **4**, 651–654 (1987).
[29]G. Indebetouw, "Nondiffracting optical fields: Some remarks on their analysis and synthesis," J. Opt. Soc. Am. A **6**, 150–152 (1989).
[30]D. MCgloin and K. Dholakia, "Bessel beams: Diffraction in a new light," Contemp. Phys. **46**, 15–28 (2005).
[31]G. Gbur and E. Wolf, "The Rayleigh range of Gaussian Schell-model beams," J. Mod. Opt. **48**, 1735–1741 (2001).
[32]J. A. A. Engelbrecht, "Modelling the reflectance of silicon," Infrared Phys. Technol. **35**, 701–708 (1994).
[33]D. W. Hahn and M. N. Özisik, *Heat Conduction* (John Wiley & Sons, New York, 2012).
[34]E. Castillo-Orozco, A. Kar, and R. Kumar, "Thermal response of Bessel beam-heated microdroplets carrying nanoparticles for deposition," in *ICALEO 2020 Conference Proceedings*, *Orlando, FL, 19 October 2020* (LIA, Orlando, 2020).